Systematic study of entrance channel effects in incomplete fusion dynamics

Anuj Kumar Jashwal[1†] Avinash Agarwal[1‡] Munish Kumar[1] Harsh Vardhan[1] Satyam Gangwar[1] Vibhuti Sinha[1]
Mohd. Faizan Khan[2] K. Kumar[3] S. Ali[4] S. Dutt[5] I. A. Rizvi[2] A. K. Chaubey[2]

[1]Department of Physics, Bareilly College, MJP Rohilkhand University Bareilly- 243006, India
[2]Department of Physics, Aligarh Muslim University, Aligarh- 202002, India
[3]Department of Physics, Hindu College, MJP Rohilkhand University Bareilly- 243006, India
[4]MANUU Polytechnic, Maulana Azad National Urdu University, Hyderabad, 500032, India
[5]Institute of Modern Physics, Chinese Academy of Sciences, Lanzhou 730000, Peoples Republic of China

Abstract: We perform a comprehensive analysis of the complete and incomplete fusion cross sections of the reaction residues produced for the ^{16}O + ^{93}Nb system at energies above the barrier, with a novel interpretation in terms of entrance channel parameters. The measured excitation functions of the residues have been compared with the predictions of the statistical model code PACE4 to understand the reaction mechanisms associated with the energy region of interest. The experimental cross sections of ^{106}In, ^{105}Cd, and ^{104}Cd residues measured at varying projectile energies are populated to a large extent through the complete fusion processes. However, a noticeable cross-section enhancement in the α-emitting channels has been observed compared to statistical model predictions. The observed enhancement may be attributed to the involvement of breakup fusion processes. To shed light on the onset and strength of incomplete fusion, the incomplete fusion fraction has been derived as a function of various entrance channel parameters. Further, the total fusion cross sections of three systems, ^{18}O + ^{93}Nb, ^{16}O + ^{93}Nb (present work), and ^{13}C + ^{93}Nb, have been reduced using standard reduction procedures, which show that the incomplete fusion fraction for reactions induced by projectile ^{16}O has a lower value compared to reactions induced by ^{18}O and a larger value when compared to reactions induced by ^{13}C. This reduction method undeniably reveals the projectile type dependency of incomplete fusion reactions, and the results may be explained by considering the projectile Q_α value. In addition, the dependence of incomplete fusion dynamics on the total asymmetry parameter, system parameter, fissility parameter, nuclear potential parameters, and target deformation is extensively investigated. Suppression in the fusion cross section is found when compared to the universal fusion function.

Keywords: Heavy-ion-induced reactions, stacked foil activation technique, PACE4 code, entrance channel parameters

DOI: 10.1088/1674-1137/ae6b1f **CSTR:**

I. INTRODUCTION

Over the past several decades, a thorough examination of the fusion reactions of tightly and weakly bound stable heavy projectiles with medium and heavy targets has been performed and discussed in the literature [1−5]. However, the mechanisms behind various reaction processes, such as complete fusion (CF), incomplete fusion (ICF), deep inelastic scattering, quasi-fission, precompound processes near the Coulomb barrier, and nucleon transfer reactions, which are likely to be observed in low-energy heavy ion-induced reactions, have not yet been completely understood [6−11]. Despite this, their importance in understanding the synthesis of super-heavy elements [12, 13], the quantum mechanical tunneling phenomenon near sub-barrier energies, the fusion hindrance phenomenon at deep sub-barrier energies [14, 15], and the behavior of nuclei far from the stability region investigated using radioactive ion beams on medium/heavy mass targets [16−18], etc., has fascinated researchers for further studies. Due to the limited availability of intense exotic beams, researchers have conducted extensive experimental studies using intense beams of stable weakly bound nuclei ^{6,7}Li, and ^{9}Be, as well as tightly bound nuclei ^{12}C, ^{16}O, and ^{19}F [19−24]. The effects of tightly and weakly bound (stable, halo, and Borromean) nuclei on the interaction phenomena are surprisingly distinct [25]. Tightly bound nuclei (^{12}C, ^{16}O) may transfer their full momentum to the target, resulting in complete fusion. On the other hand, weakly bound nuclei (like ^{6,7}Li, and ^{9}Be)

Received 20 January 2026; Accepted 8 May 2026
† E-mail: anuj3674@gmail.com
‡ E-mail: corresponding author: avibcb@gmail.com

may break up into one or more fragments before fusing with the target [19−21]. This phenomenon, known as break-up fusion or incomplete fusion, results in a partial amount of momentum transfer. Reduced incoming flux leads to the formation of a compound nucleus with lower mass and excitation energy, which in turn affects the production cross section of individual evaporation residues. In heavy ion collisions, particularly induced by light and/or heavy weakly bound nuclei, the breakup cross sections are typically very large, and breakup coupling can have a significant effect on the cross sections of several other channels [26−28].

Recently, many efforts have been made to comprehend the low-energy ICF processes and their sensitivity to different entrance channel parameters [29−32]. Our research collaborators have also been engaged in investigating the dynamics of ICF reactions at low energies [33−37]. Parker et al. [38] observed the occurrence of ICF for a variety of projectiles ^{12}C, ^{15}N, ^{16}O, ^{19}F, and ^{20}Ne interacting with a ^{51}V target at energies of ≈ 6 MeV/nucleon. In addition, recent studies demonstrate that the ICF fraction is greatly influenced by both the projectile energy and its structure [33, 37]. The projectile structure effect on ICF is explored more effectively in terms of the projectile Q_α value [34]. The theory by Morgenstern et al. [39] emphasizes that the ICF fraction is influenced by the entrance channel mass asymmetry of the interacting partners. The Universal Fusion Function (UFF), proposed by Canto et al. [4], is a significant technique for studying the influence of different entrance channel characteristics on ICF dynamics. This method entails comparing the measured fusion cross sections to UFF in heavy-ion interactions. In this article, with the motivation of gaining better insight into the ICF dependence on various entrance channel parameters, the excitation functions (EFs) of evaporation residues (ERs) populated in the interaction of the ^{16}O + ^{93}Nb system have been measured in the energy range from 55.1–98.1 MeV. The measured excitation function of the residues has been studied within the framework of one of the widely used statistical model codes PACE4 [40] to understand the reaction mechanisms involved in the low energy region. It is noteworthy that Sharma et al. [41] have also investigated the same projectile-target system. The work of Sharma et al. [41] was essentially limited to reporting excitation functions of selected residues and comparing them with statistical model calculations. No attempt was made to separate independent cross sections for precursor-fed channels, and to extract the incomplete fusion fraction (F_{ICF}) along with its dependency on entrance channel parameters. Consequently, the present study addresses the systematic behavior of ICF over the work reported by Sharma et al. [41] for this system.

In view of this, the present work not only supplements the data of earlier work [41], but also provides a better presentation of the excitation function measurements of the ERs. Independent cross sections have been deduced to remove precursor contributions, enabling a more reliable estimation of α-emitting channel strengths. The ICF cross sections and F_{ICF} values have been quantitatively extracted over the entire energy range. Most importantly, the present work undertakes a systematic and comprehensive correlation analysis, exploring the dependence of ICF strength on entrance channel parameters, such as projectile energy, projectile Q_α value, total asymmetry, system parameter (ζ), fissility, nuclear potential parameters, target deformation, and complete fusion suppression analyzed within the Universal Fusion Function framework. Furthermore, by incorporating the ^{16}O + ^{93}Nb system into the systematic framework previously established for ^{13}O + ^{93}Nb [33] and ^{18}O + ^{93}Nb [37] systems, the present study completes the sequence of three projectiles on the same target. This controlled comparison significantly reduces target-dependent ambiguities and provides a more stringent test of projectile-structure and breakup-threshold effects on ICF dynamics. Therefore, the present investigation does not merely extend earlier measurements, but substantially advances the systematic understanding of low-energy incomplete fusion processes. The paper presents the experimental methodology and data reduction procedures in Sec. II, while Sec. III deals with the analysis of the data with the help of nuclear model code, and Sec. IV demonstrates the influence of ICF on CF and its dependency on various entrance channel parameters. Section V gives a summary of the work done and the conclusions.

II. EXPERIMENTAL METHODOLOGY

The present experiment was designed and performed using the 15UD Pelletron accelerator at the Inter-University Accelerator Centre (IUAC), New Delhi (India), employing a methodology similar to that of our earlier publications [33, 37]. Self-supporting targets of natural ^{93}Nb were prepared using a rolling mill in the target laboratory of IUAC, New Delhi. Nb foils (1.712 mg/cm^2) stacked alternately with the ^{27}Al catcher foils (2.078 mg/cm^2) were arranged in front of the ^{16}O beam. The uniformity of each target was confirmed by the α-transmission method. Al-catcher foils were used for capturing the recoiling ERs and for energy degradation to achieve a desired range of energy interest. Based on the available beam intensity and the expected number of events for each channel, irradiation was performed for approximately 8–10 hours in the general-purpose scattering chamber. An in-vacuum transfer facility was used to reduce the time between the end of irradiation and the start of counting. The weighted average beam current of ≈ 25–30 nA was calculated with an electron-suppressed Faraday cup, employing a precise current integrator device. Beam fluxes recorded using two different techniques (time-weighted beam current and total charge collected in the

Faraday cup) were found to be consistent within a 10% variation. A Monte Carlo simulation-based SRIM code [42] was used to determine the amount of energy lost with each target. The energy (E) used for analysis was the average of the incident and outgoing energies.

After the irradiation, the stack of Al catchers along with the ^{93}Nb target was taken out from the scattering chamber with the help of an in-vacuum transfer facility. The activities induced in the target catcher assembly were recorded separately by a pre-calibrated, high-resolution, high-purity germanium (HPGe) detector coupled with the computer-automated measurement and control-based data acquisition system CANDLE [43] software. The target-catcher foil collections underwent several rounds of counting: first, for short periods of time (i.e., ≈ 100–300 s) to capture the reaction products with short half-lives, and then for longer periods of time (i.e., ≈ 10–60 minutes) to identify reaction products with relatively long half-lives. The Ge crystal (a part of the detector) was protected from outside sources of radiation by a lead brick shield of sufficient thickness. The absolute efficiency and energy calibration of the detectors were determined using a set of standard radioactive sources of ^{152}Eu ($T_{1/2}$ = 13.517 yr) and ^{133}Ba ($T_{1/2}$ = 10.551 yr) at the target position. A typical profile of γ-ray for the ^{16}O + ^{93}Nb system at an incident energy of 79.3 ± 1.0 MeV is shown in Fig. 1, where the characteristic peaks are marked with corresponding decaying channels. The evaporation residues are confirmed not only by their characteristic γ-ray energies but also by their decay data. The nuclear spectroscopic data used to calculate the cross sections are tabulated in Table 1 and are taken from the Table of Radioactive Isotopes [44]. Further, the decay curves of the reaction residue ^{104}Cd formed via the p4n channel, identified with two different γ rays of 83.6 and 709.3 keV, are given in Fig. 2. It can be seen in Fig. 2 that the half-life of ^{104}Cd(p4n) determined from the decay curves agrees well with the value given in the literature (57.7 min) [44] within the limit of experimental uncertainty. This verifies the production of the residue ^{104}Cd via the p4n channel. The other residues were identified by applying the same method. Using the standard formulation [33], we calculated the production cross sections for the identified reaction residues populated via CF and/or ICF reactions at each energy:

$$\sigma(\mathrm{E}) = \frac{\mathrm{A}\lambda\exp(\lambda \mathrm{t}_2)}{\mathrm{N}_0\phi\epsilon_\mathrm{G}\theta\mathrm{K}[1-\exp(-\lambda \mathrm{t}_1)][1-\exp(-\lambda \mathrm{t}_3)]}$$

where A is the total number of counts recorded under the peak in time t_3, N_0 is the number of target nuclei per area, ϕ is the incident flux, t_1 is the irradiation time, t_2 is the time elapsed between the stop of irradiation and the start of counting, t_3 is the counting time, θ is the branching ratio, λ is the decay constant of the evaporation residue, ϵ_G is the geometry-dependent efficiency of the HPGe detector, and K is the self-absorption correction factor of the γ-ray in the target. The evaporation residue (ER) cross-section has been calculated using the EXPSIGMA code, written based on the above formulation. The possible sources of the associated measurement uncertainties in the cross-section are as follows: (i) variations of 2% in the geometry-dependent efficiency of the detector, (ii) inaccuracy in the measurement of target thickness leading to an error of 2%, and (iii) incident flux may change due to fluctuations in beam current during irradiation. The beam current has been carefully maintained, and the error due to beam fluctuations is predicted to be less than 6%. (iv) By properly adjusting the source-detector distance, the dead time of the spectrometer was kept to a minimum. Additionally, a 50 Hz pulser was used to accurately estimate the dead time of the detector. Efforts were taken to minimize the uncertainties caused by all the above factors. Errors in the present measurements, including the above-mentioned sources of uncertainties, are estimated to be ⩽15%.

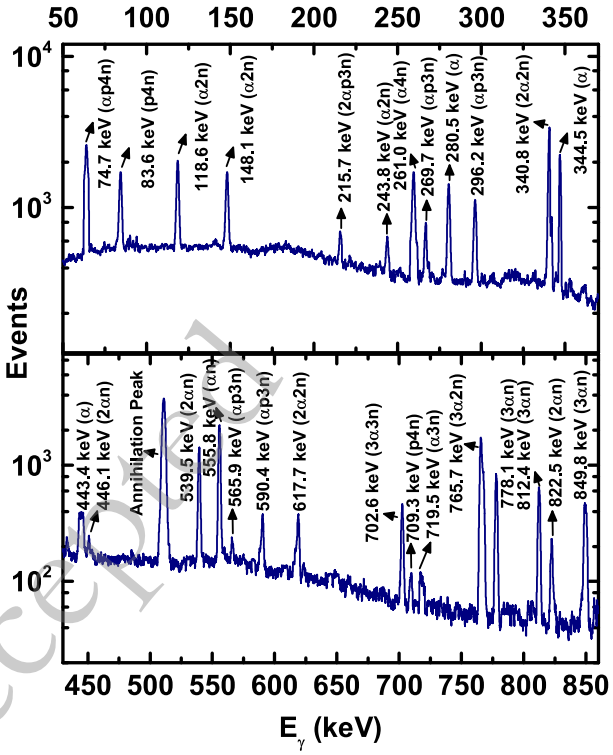

Fig. 1. (color online) Typical γ-ray energy spectrum obtained from the interaction of the ^{16}O + ^{93}Nb system at E_{lab} = 79.3 ± 1.0 MeV. Some of the identified γ-ray peaks have been assigned to the respective evaporation residues populated via CF and/or ICF channels.

III. DATA EXTRACTION, ANALYSIS, AND INTERPRETATION

In the present experimental study, EFs of ERs,

Table 1. Identified evaporation residues produced in the ^{16}O + ^{93}Nb system are listed along with their half-lives, decay modes, characteristic γ-ray energies, and dominant production reaction channels.

Nuclides	Half-life	Decay mode	E_γ (keV)[I_γ (%)]	Production reaction channel
^{106}In	6.2 min	$\epsilon^a+\beta^+(100)$	861.1[92.0]	^{93}Nb(^{16}O,3n)
^{105}Cd	55.5 min	$\epsilon+\beta^+(100)$	961.8[4.6]	^{93}Nb(^{16}O,p3n)
^{104}Cd	57.7 min	$\epsilon+\beta^+(100)$	83.6[47.0],709.3[19.5]	^{93}Nb(^{16}O,p4n)
^{105}Ag	41.29 d	$\epsilon+\beta^+(100)$	280.5[31.0],344.5[42.0] 443.4[10.7]	^{93}Nb(^{16}O,α)
^{104}Ag	1.153 h	$\epsilon+\beta^+(100)$	555.8[92.8],857.9[10.3] 926.0[12.5],941.7[25.2]	^{93}Nb(^{16}O,αn)
^{103}Ag	65.7 min	$\epsilon+\beta^+(100)$	118.6[31.2],148.1[28.3] 243.8[8.5]	^{93}Nb(^{16}O,α2n)
^{102}Ag	12.9 min	$\epsilon+\beta^+(100)$	719.5[58.0]	^{93}Nb(^{16}O,α3n)
^{101}Ag	11.1 min	$\epsilon+\beta^+(100)$	261.0[52.6]	^{93}Nb(^{16}O,α4n)
^{101}Pd	8.47 h	$\epsilon+\beta^+(100)$	269.7[6.4],296.2[19.2] 565.9[3.4],590.4[12.0]	^{93}Nb(^{16}O,αp3n)
^{100}Pd	3.63 d	$\epsilon(100)$	74.7[98.0]	^{93}Nb(^{16}O,αp4n)
^{100}Rh	20.8 h	$\epsilon+\beta^+(100)$	446.1[11.2],539.5[78.4] 822.5[20.0]	^{93}Nb(^{16}O,2αn)
^{99m}Rh	4.7 h	$\epsilon+\beta^+(>99.84)$,IT^b(<0.16)	340.8[69.0],617.7[11.8] 1261.0[10.9]	^{93}Nb(^{16}O,2α2n)
^{97}Ru	2.88 d	$\epsilon(100)$	215.7[86.0]	^{93}Nb(^{16}O,2αp3n)
^{96}Tc	4.28 d	$\epsilon+\beta^+(100)$	778.1[99.7],812.4[82.0] 849.8[98.0]	^{93}Nb(^{16}O,3αn)
^{95}Tc	20.0 h	$\epsilon+\beta^+(100)$	765.7[94.0],947.6[1.9]	^{93}Nb(^{16}O,3α2n)
^{94}Tc	293 min	$\epsilon+\beta^+(100)$	702.6[99.6],871.1[99.9]	^{93}Nb(^{16}O,3α3n)

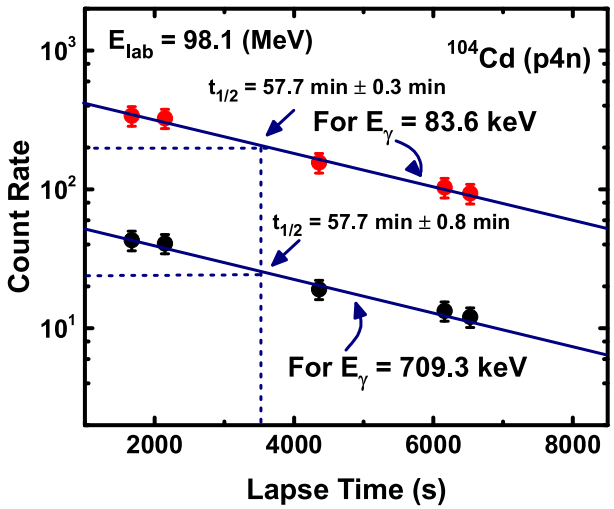

Fig. 2. (color online) Decay curve of the reaction residue ^{104}Cd(p, 4n) for 83.6 keV and 709.3 keV γ-ray energy.

namely, ^{106}In, ^{105}Cd, ^{104}Cd, ^{105}Ag, ^{104}Ag, ^{103}Ag, ^{102}Ag, ^{101}Ag, ^{101}Pd, ^{100}Pd, ^{100}Rh, ^{99m}Rh, ^{97}Ru, ^{96}Tc, ^{95}Tc, and ^{94}Tc have been populated through CF and/or ICF channels in the ^{16}O + ^{93}Nb system at energies 55.1–98.1 MeV. These measured excitation functions have been investigated within the framework of one of the widely used statistical model codes, PACE4 [40]. This code is based on the Hauser-Feshbach theory of compound nucleus (CN) decay and employs a statistical approach to CN de-excitation via the Monte Carlo procedure [45]. The angular momentum projections are taken at each stage of de-excitation. The cross-sections for a particular reaction channel are calculated using Bass formulations [46]. Partial cross-section (ℓ) for CN formation as a function of incident energy and angular momentum (σ_ℓ) values is:

$$\sigma_\ell = \frac{\lambda^2}{4\pi}(2\ell+1)\mathrm{T}_\ell$$

where λ is the reduced wavelength, and the transmission coefficient (T_ℓ) is considered to be

$$\mathrm{T}_\ell = \left[1+\exp\left(\frac{\ell-\ell_{\max}}{\Delta}\right)\right]^{-1}$$

where Δ is the diffuseness parameter, and ℓ_{max} is the maximum value of ℓ determined by the total CF cross-section.

$$\sigma_F = \sum_{\ell}^{\infty} \sigma_\ell$$

The transmission coefficients for light emitted particles such as neutrons (n), protons (p), and alpha particles (α) are calculated using optical model potentials (OMP). In Hauser-Feshbach calculations at low energies, the potential provided by Wilmore and Hodgson [47] is used as the neutron potential instead of the one provided by Becchetti-Greenlees [48].

The neutron potential and other OMP parameters are given in MeV for potentials and in fm for radius.

$$V = 47.01 - 0.267E - 0.00018E^2$$

$$r_0 = 1.322 - 7.6A \times 10^{-4} + 4A^2 \times 10^{-6} - 8A^3 \times 10^{-9}$$

$$a_0 = 0.66$$

$$W_D = 9.52 - 0.053E$$

$$r_D = 1.266 - 3.7A \times 10^{-4} + 2A^2 \times 10^{-6}$$

$$a_D = 0.48$$

The OMP parameters for the proton are

$$V = 53.3 - 0.55E - 27(N-Z)/A + 0.4(Z/A^{1/3})$$

$$r_0 = 1.25, a_0 = 0.66$$

$$W_D = 13.5 \pm 2.0$$

$$r_D = 1.25, a_D = 0.47$$

$$V_{SO} = 7.55, r_{SO} = 1.064, a_{SO} = 0.78$$

$$r_C = 1.25$$

For α particles, PACE4 [40] uses OMP parameters that are fixed. The OMP parameters for α particles

$$V = 50, r_0 = 1.17A^{1/3} + 1.77, a_0 = 0.576$$

$$W_D = 45.7\exp(-x), \text{where } x = (r - 1.40A^{1/3})/a_D$$

$$r_D = 1.17A^{1/3} + 1.77$$

$$a_D = 0.576$$

In this code, the level density $a = A/K\,\mathrm{MeV}^{-1}$ is another important parameter of the statistical code, where K is the free parameter. To match the experimentally measured cross sections of the ERs, the value of "K" can be adjusted within the physically acceptable limitations [49]. Gilbert et al. [50] show that the choice of K above 10 is unreasonable, but it has been observed in recent studies [51] that $K = 13$ and $K = 10$ satisfactorily reproduce the experimental data for complete fusion channels over a broad energy range for ^{9}Be + ^{169}Tm and ^{9}Be + ^{187}Re respectively. Also, for the ^{20}Ne + ^{165}Ho system [52], the authors claim that a level density parameter constant $K = 12$ reproduces the measured EFs satisfactorily for the reaction channels populated via the CF process. Although it is feasible to elucidate all excitation functions by varying the parameters of the code for each channel, such an approach is fundamentally unreasonable from a physics perspective. Further, other reports [31, 33, 36, 37] are also available in the literature where the value of the level density parameter for statistical model calculations has been optimized with experimental observations for the reaction channels expected solely via CF dynamics, and the optimized parameter thus obtained has been used for further analysis of the particular projectile-target system. It is also important to mention here that the code PACE4 does not take ICF into account, so any enhancement in the experimentally measured EFs over the theoretical predictions gives a clear indication of incomplete fusion [22–24]. The experimentally measured cross section data are presented in Tables 2 and 3. The residues produced through various reaction channels in the ^{16}O + ^{93}Nb system are explained below.

A. Excitation function measurement of x*n* and $p \times n$ emitting channels

In order to better understand the reaction mechanism of evaporation residues populated via x*n* and/or *p*x*n* channels, an attempt has been made to reproduce the measured EFs of these evaporation residues using the statistical model code PACE-4. The experimentally measured EFs of ^{106}In, ^{105}Cd, and ^{104}Cd are expected to be populated through the complete fusion process. To determine the suitable value of the level density parameter,

Table 2. Experimentally measured production reaction cross sections of the evaporation residues ^{106}In, ^{105}Cd, and ^{104}Cd populated in the ^{16}O + ^{93}Nb system at different projectile energies.

E_{lab} (MeV)	$\sigma(^{106}\text{In})$ (mb)	$\sigma(^{105}\text{Cd})$ (mb)	$\sigma(^{104}\text{Cd})$ (mb)
98.1 ± 1.2	0.3 ± 0.07	20.2 ± 2.6	335.6 ± 43.6
89.9 ± 1.1	1.0 ± 0.16	129.5 ± 16.8	299.7 ± 38.9
79.3 ± 1.0	19.5 ± 2.9	400.4 ± 52.0	41.39 ± 5.3
67.8 ± 1.3	171.0 ± 25.6	147.8 ± 19.2	–
55.1 ± 1.2	65.8 ± 9.7	–	–

different values of K (8, 10, and 12) have been tested. As a representative case, the effect of variation of the parameter K on measured EFs of the ERs ^{106}In is reported in Fig. 3. This figure also displays the results obtained by Sharma et al. [41] for the same system. As can be seen from this figure, the experimentally measured excitation functions for the 3n channel are in good agreement with the theoretical predictions at K=8, except at an energy of 98.1 MeV. At the higher energy point, the cross-section value matches with K=10. However, the results obtained by Sharma et al. [41] significantly mismatch the present data. The same difference has also been observed for the cross-section values of the same 3n channel reported by the same group [53] for another system in the study reported by Chauhan et al. [54]. The observed difference in the results might be due to the variation of the offline counting statistics because of the very short half-life (6.2 min) of ^{106}In. Furthermore, the experimentally measured and PACE4-calculated ratio of $\sigma_{p4n}/\sigma_{p3n}$ as a function of E_{lab} is given in Fig. 4. For the ratio of $\sigma_{p4n}/\sigma_{p3n}$, PACE4 with K=8 is in good agreement with the experimental data throughout the energy range. Since the PACE4 calculations are based on compound nucleus theory and do not take the ICF into account, it is evident that the evaporation residues ^{106}In, ^{105}Cd, and ^{104}Cd are clearly formed by de-excitation of the compound nucleus ^{109}In* through x*n* and/or *pxn* channels. This is in accordance with the statement reported in earlier publications [31, 33, 36, 37]. Furthermore, no contribution of ICF to the formation of ^{106}In, ^{105}Cd, and ^{104}Cd can be claimed in the considered energy range. The experimentally measured reaction cross-sections for x*n* and/or *pxn* channels are presented in Table 2.

B. Evaporation residues populated through the *α*-emitting channels

The ERs emerging through the *α*-emitting channels have the dual probability of being populated through both the CF process and the ICF process. The excitation functions of ERs, namely ^{105}Ag, ^{104}Ag, ^{103}Ag, ^{102}Ag, ^{101}Ag, ^{101}Pd, ^{100}Pd, ^{100}Rh, ^{99m}Rh, ^{97}Ru, ^{96}Tc, ^{95}Tc, and ^{94}Tc, are found to be populated through different *α*-emitting channels in the ^{16}O+^{93}Nb system at energies of 55.1–98.1 MeV. The experimentally measured EFs of individual *α*-

Table 3. Experimentally measured production reaction cross-sections *σ* (mb) of identified evaporation residues in the ^{16}O + ^{93}Nb system at different projectile energies.

E_{lab} (MeV)	$\sigma^{ind}(^{105}\text{Ag})$ (mb)	$\sigma^{ind}(^{104}\text{Ag})$ (mb)	$\sigma(^{103}\text{Ag})$ (mb)	$\sigma(^{102}\text{Ag})$ (mb)	$\sigma(^{101}\text{Ag})$ (mb)
98.1 ± 1.2	13.8 ± 2.3	208.3 ± 27.0	90.2 ± 11.7	32.9 ± 4.2	165.4 ± 21.5
89.9 ± 1.1	45.8 ± 7.7	192.1 ± 24.9	9.7 ± 1.2	117.3 ± 15.2	105.4 ± 13.7
79.3 ± 1.0	91.7 ± 15.5	56.4 ± 7.3	18.9 ± 2.4	164.2 ± 21.3	10.6 ± 1.3
67.8 ± 1.3	42.5 ± 7.2	10.6 ± 1.3	76.9 ± 10.0	45.3 ± 5.8	–
55.1 ± 1.2	5.4 ± 0.92	11.7 ± 1.5	75.1 ± 9.7	–	–
E_{lab} (MeV)	$\sigma^{ind}(^{101}\text{Pd})$ (mb)	$\sigma(^{100}\text{Pd})$ (mb)	$\sigma(^{100}\text{Rh})$ (mb)	^{99m}Rh (mb)	$\sigma(^{97}\text{Ru})$ (mb)
98.1 ± 1.2	219.4 ± 28.5	65.1 ± 8.4	9.2 ± 1.2	9.6 ± 1.2	20.8 ± 0.65
89.9 ± 1.1	145.0 ± 18.8	10.8 ± 1.4	3.8 ± 0.50	20.6 ± 2.7	12.6 ± 1.6
79.3 ± 1.0	9.2 ± 1.1	1.5 ± 0.20	4.9 ± 0.64	22.2 ± 2.8	5.7 ± 0.74
67.8 ± 1.3	–	1.0 ± 0.13	6.2 ± 0.81	9.5 ± 1.2	8.8 ± 1.8
55.1 ± 1.2	–	–	–		–
E_{lab} (MeV)	$\sigma(^{96}\text{Tc})$ (mb)	$\sigma(^{95}\text{Tc})$ (mb)	$\sigma(^{94}\text{Tc})$ (mb)		
98.1 ± 1.2	5.0 ± 0.65	6.4 ± 0.8	3.4 ± 0.45		
89.9 ± 1.1	3.8 ± 0.50	3.1 ± 0.41	1.3 ± 0.16		
79.3 ± 1.0	2.0 ± 0.26	1.5 ± 0.20	0.5 ± 0.07		
67.8 ± 1.3	1.2 ± 0.16	–	1.2 ± 0.1		
55.1 ± 1.2	–	–	–		

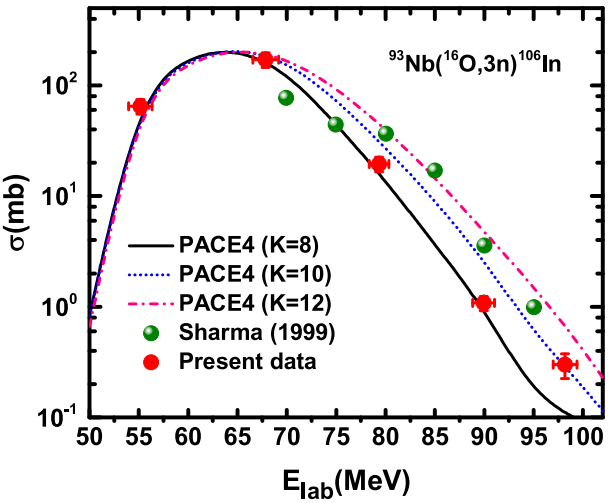

Fig. 3. (color online) Comparison of experimentally measured cross-sections of ^{106}In with the results obtained from PACE4 calculations for different values of the level density parameter (a = A/K MeV^{-1}, where K = 8, 10, and 12) is presented. Solid (red) circles with error bars in incident energy and cross-sections are the results of the present work, and solid (green) circles represent the work of Sharma et al. [41].

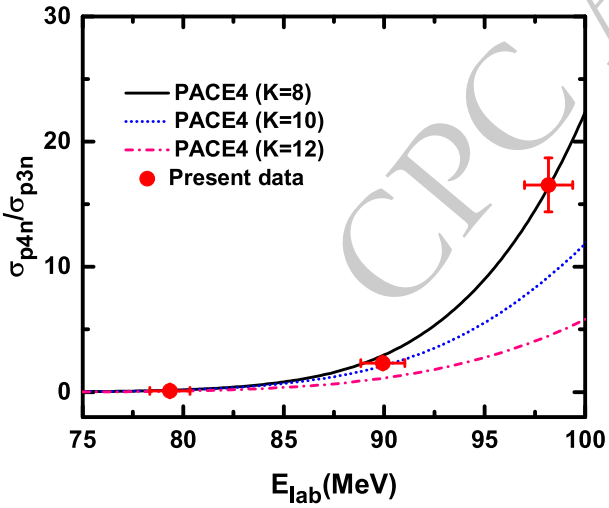

Fig. 4. (color online) Variation of the cross-section ratio σ_{p4n} to σ_{p3n} with energy E_{lab} for the ^{16}O + ^{93}Nb system. The experimental data are compared with PACE4 statistical model calculations using different level density parameters $K = 8$, 10, and 12.

emitting channels are compared with PACE4 predictions using the same set of parameters. It is worth emphasizing that the experimentally measured cross sections for the ERs ^{105}Ag, ^{104}Ag, and ^{101}Pd are strongly fed from their higher charge precursor isobars, ^{105}Cd, ^{104}Cd, and ^{101}Ag, respectively, through an electron capture (EC) process and/or β^+ emission. The independent cross sections (σ_{ind}) have been calculated from the cumulative cross sections (σ_{cum}) using the Cavinato et al. [55] formulation given as

$$\sigma_{ind} = \sigma_{cum} - P_{pre}\left[\frac{t^D_{1/2}}{t^D_{1/2} - t^P_{1/2}}\right]\sigma_P$$

Here σ_P is the production cross-section of the precursor or parent nuclei, $t^D_{1/2}$ and $t^P_{1/2}$ are the half-lives of the daughter and precursor nuclei, respectively. The P_{pre} is the branching ratio of the precursor to its daughter nuclei.

The values of σ_{cum} and σ_{ind} along with the results of Sharma et al. [41] for ^{105}Ag are given in Fig. 5(a). However, Sharma et al. [41] did not calculate independent cross sections for this channel in their results. The cumulative production of ^{105}Ag has also been reported by Agarwal et al. [37] recently. In contrast, measurement by Sharma et al. [41] showed a large difference in cross-section compared to PACE4, where a difference of hundreds/tens of mb for ^{105}Ag has been fully attributed to the sum (ICF+transfer). Similarly, the experimentally measured EFs of the residues ^{104}Ag, ^{103}Ag, ^{102}Ag, ^{101}Ag, ^{101}Pd, ^{100}Pd, ^{100}Rh, and ^{99m}Rh, populated through α or 2α emitting channels, also show an enhancement over the PACE4 predictions even after removing precursor contributions in the case of ^{104}Ag and ^{101}Pd channels. This indicates the production of these ERs through CF as well as ICF throughout the energy range.

It is interesting to note that the ER ^{101}Pd may be populated via three different reaction routes represented as follows:

(a) CF of ^{16}O with ^{93}Nb:

$$^{16}\mathrm{O} + {}^{93}\mathrm{Nb} \Rightarrow {}^{109}\mathrm{In}^{*} \Rightarrow {}^{101}\mathrm{Pd} + \alpha + \mathrm{p} + 3\mathrm{n}$$

(b) ICF of ^{16}O with ^{93}Nb:

$$^{16}\mathrm{C}(^{12}\mathrm{C} + {}^{4}\mathrm{He}\ \text{or}\ \alpha) + {}^{93}\mathrm{Nb} \Rightarrow {}^{105}\mathrm{Ag} + \alpha\ (\text{Spectator})$$

$$^{105}\mathrm{Ag} \Rightarrow {}^{101}\mathrm{Pd} + \mathrm{p} + 3\mathrm{n}$$

(c) EC/β^+ decay of the precursor isobar

$$^{16}\mathrm{O} + {}^{93}\mathrm{Nb} \Rightarrow {}^{109}\mathrm{In}^{*} \Rightarrow {}^{105}\mathrm{Cd} + \mathrm{p} + 3\mathrm{n}$$

$$^{105}\mathrm{Cd} \Rightarrow EC/\beta^{+} {}^{105}\mathrm{Ag}$$

Further, Fig 5(b) shows the experimentally measured EFs of residue ^{97}Ru, where the theoretical predictions made by the PACE4 code give negligible cross sections and are not displayed here. This suggests that the ^{97}Ru residue is only contributed by the ICF process. It is important to note that the measured EF of ^{97}Rh has been reported for the first time in this study using this reaction

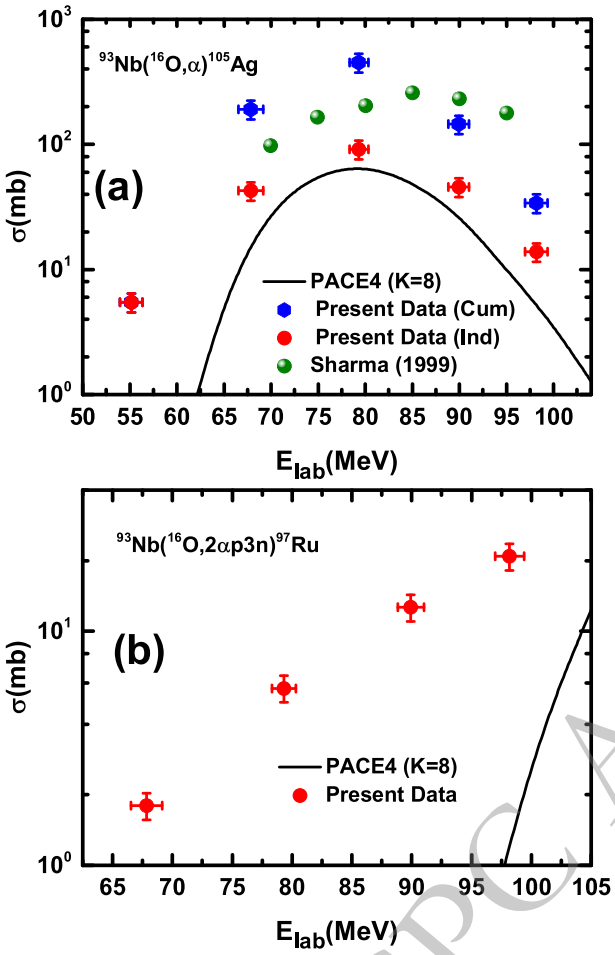

Fig. 5. (color online) (a) Comparison of experimentally measured cross sections of ^{105}Ag with the results obtained from PACE4 calculations for different values of the level density parameter ($a = A/8$ MeV^{-1}). Solid (blue) and (red) circles represent the measured cumulative and independent cross sections for the present study, respectively. Solid (green) circles represent the work of Sharma et al. [41]. (b) Comparison of experimentally measured cross sections of ^{97}Ru with the results obtained from PACE4 calculations for different values of the level density parameter ($a = A/8$ MeV^{-1}).

pathway. However, the experimentally measured EFs of the residues ^{96}Tc and ^{95}Tc significantly underestimate the PACE4 predictions, and for ^{94}Tc, PACE4 gives negligible cross-sections. Consequently, it may be noted that the contribution of these residues is fed via the ICF process. The experimentally measured reaction cross sections of the observed ERs populated through α-emitting channels are given in Table 3.

IV. EFFECT OF ENTRANCE CHANNEL PARAMETERS ON ICF

The dependence of ICF dynamics on various entrance channel parameters has been explored by a number of researchers [23, 31, 35–37]. It is now well documented that the ICF fraction greatly depends on various entrance channel parameters, namely: projectile energy, projectile structure, mass asymmetry of interacting partners, Coulomb factor, projectile Q_α value, and neutron skin thickness of the target. The role of ICF processes in the formation of all the α-emitting channels has been calculated by subtracting the PACE4 contributions for all α-evaporating channels from the total experimentally measured EFs for α-channels. As such, the ICF cross section has been calculated at each projectile energy as $\Sigma\sigma_{ICF} = \Sigma\sigma_{Expt.} - \Sigma\sigma_{PACE}$. To investigate the dependence of ICF on various entrance channel parameters, the ICF fraction or ICF probability, $F_{ICF}(\%)$, for the ^{16}O+^{93}Nb system has been calculated. The $F_{ICF}(\%)$ is a measurement of the strength of the ICF relative to total fusion ($\sigma_{TF} = \Sigma\sigma_{CF} + \Sigma\sigma_{ICF}$) and is defined as $[F_{ICF}(\%) = \left(\frac{\Sigma\sigma_{ICF}}{\sigma_{TF}}\right) \times 100]$. It is worth mentioning that the difference between the experimental cross-sections and the PACE4 predictions ascribed solely to incomplete fusion represents an approximation. The PACE4 code, based on the statistical Hauser–Feshbach formalism, involves model-dependent parameters such as level densities and transmission coefficients, which may introduce uncertainties in the calculated channel strengths, particularly in the near-barrier region where the influence of dynamical effects can be more pronounced. Consequently, the extracted $F_{ICF}(\%)$ values should be regarded as effective estimates rather than absolute quantities. Nevertheless, since the same analysis methodology has been consistently adopted in analyzing the experimental data for all systems considered in the present study, the observed systematic trends and comparative behavior of F_{ICF} remain qualitatively reliable. Further, the variation of $F_{ICF}(\%)$ in terms of relative velocity (V_{rel}/c) has been plotted and displayed in Fig. 6. The following expression has been considered for the calculation of relative velocity:

$$V_{rel} = \sqrt{2(E_{c.m.} - V_{CB})/\mu}$$

where μ is the reduced mass of the system, $E_{c.m.}$ is the center of mass energy for the reaction, and V_{CB} is the Coulomb barrier between two interacting partners. A widely used value of V_{rel}, i.e., 0.053c, is considered to be the lower limit by Morgenstern et al. [39] for establishing incomplete fusion. Fig. 6 shows that F_{ICF} increases with V_{rel}, and its contribution is also found to be considerably below the limit of $V_{rel} = 0.053c$. Based on the observed behavior of F_{ICF}, ICF contributions are likely to increase from $V_{rel} \approx 0.02c$ to 0.08c. The same trend has also been observed earlier for α cluster projectiles like ^{12}C [56], ^{16}O [36], and ^{18}O [37]. The role of various en-

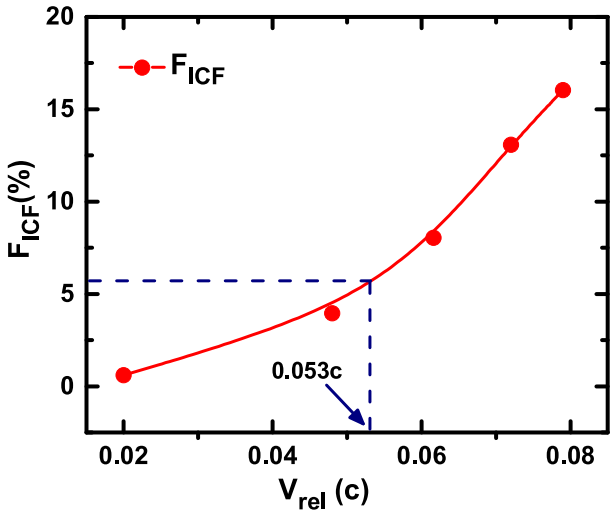

Fig. 6. (color online) Variation of the deduced incomplete fusion fraction, F_{ICF}(%), as a function of the effective relative velocity, V_{rel} (c), for the ^{16}O + ^{93}Nb system. The solid curve through the experimental data points represents the best fit to the data points.

trance channel parameters on the ICF reaction dynamics will be examined in the following subsections.

A. ICF dependence on projectile structure

Recent studies on heavy ion interactions indicate that the geometric aspects of various systems can be affected by reducing the center of mass energy and fusion cross-sections [5]. A direct comparison of the fusion cross-sections involved in the various reaction processes for systems with different projectiles and forming different compound nuclei may lead to misinterpretation of the experimental results. In this regard, to understand the role of different projectiles on ICF reactions at low beam energy, the measured TF and ICF cross-sections in reduced scale for the present ^{16}O + ^{93}Nb system along with ^{18}O + ^{93}Nb [37] and ^{13}C + ^{93}Nb [33], have been shown in Figs. 7(a)-7(d). The reduction process eliminates the Coulomb barrier effect and the geometrical size of the interacting nuclei for the presently studied projectile-target combinations. The projectiles ^{18}O, ^{16}O, and ^{13}C have different breakup thresholds. Two different reduction methodologies have been employed to compare these experimental data on reduced scales. In the first reduction process, the reduced cross-section and energy are given by $\sigma_{\rm Red} = \sigma^{\rm Fus}_{\rm expt}/(A_{\rm P}^{1/3} + A_{\rm T}^{1/3})^2$ and $E_{\rm Red} = E_{\rm c.m.}(A_{\rm P}^{1/3} + A_{\rm T}^{1/3})/(Z_{\rm P}Z_{\rm T})$, where $Z_{\rm P}$ and $Z_{\rm T}$ represent the charge of the projectile and target, and $E_{c.m.}$ is the center of mass energy [5]. In the second case of the reduction process, the reduced cross-sections are taken to be the division of the cross-section by the quantity πR_B^2, where R_B is the barrier radius, and reduced energies are taken to be "$E_{c.m.} - V_B$". A Woods Saxon form using the Akyuz-Winther potential parameterization [57] was used for the potential parameters V_B = 43.51 MeV and R_B = 10.12 fm. From Figs. 7(a)-7(b), it can be noted that the TF as well as ICF cross-sections for ^{16}O + ^{93}Nb are less than for ^{18}O + ^{93}Nb and larger than for the ^{13}C + ^{93}Nb system. This may be due to the lower value of the breakup threshold for ^{16}O as compared to ^{18}O and a larger value as compared to the ^{13}C projectile. Hence, the present results indicate that the probability of ICF is also affected by projectile structure (α and non-α clusters). These reduction procedures are also crucial for understanding how projectile structure affects low energy ICF dynamics.

B. ICF dependence on projectile Q_α value

This subsection examines the influence of the projectile Q_α value on incomplete fusion dynamics at near-barrier energy. Figure 8 illustrates the variation of F_{ICF}(%) with the projectile Q_α for the systems ^{13}C + ^{93}Nb [33], ^{16}O + ^{93}Nb (present work), and ^{18}O + ^{93}Nb [37] at constant relative velocities V_{rel} = 0.071c and 0.053c. The Q_α values [Q_α(^{16}O) =-7.16 MeV; Q_α(^{13}C) =-10.65 MeV; Q_α(^{18}O) =-6.22 MeV] are different. Despite the observable association, Q_α should not be construed as a direct physical cause of incomplete fusion. A favorable Q_α value indicates the energetic closeness of the nucleus to a cluster-decay configuration that includes an α-particle and the residual nucleus, and is associated with the effective α-separation energy, which determines the threshold for α-breakup within the nuclear field of the target [58]. In cluster structure models, the probability of breakup in the contact region is contingent upon the preformation of α-like configurations and the energy necessary for projectile dissociation. A relatively lower effective breakup threshold can increase the probability of projectile fragmentation before complete fusion, thereby aiding in incomplete fusion. The observed pattern, as shown in Fig. 8, indicates that projectile structural effects significantly influence incomplete fusion dynamics rather than Q_α alone. These findings are in agreement with earlier studies [23, 31, 59, 60].

C. ICF dependence on total asymmetry parameter ($\alpha_{\rm total}$)

Efforts have been made to understand the behavior of ICF with entrance channel total asymmetry ($\alpha_{\rm total}$) between interacting partners. The total asymmetry parameter of the system ($\alpha_{\rm total}$) can be defined by the following equation:

$$\alpha_{\rm total} = \alpha_{\rm mass}\alpha_{\rm charge}$$

where $\alpha_{\rm mass} = \dfrac{(A_{\rm T} - A_{\rm P})}{(A_{\rm T} + A_{\rm P})}$ is the mass-asymmetry and

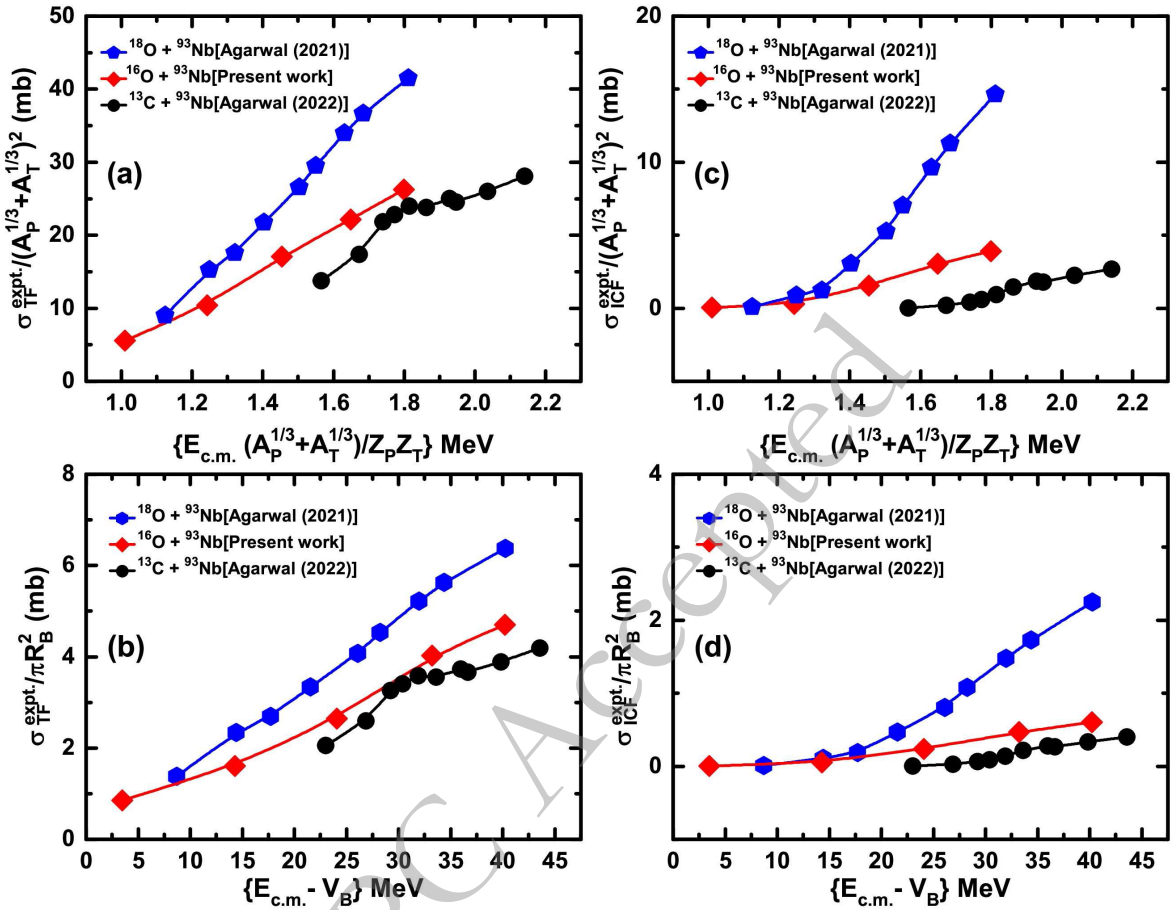

Fig. 7. (color online) Reduced total fusion and incomplete fusion cross-sections for the systems ^{18}O + ^{93}Nb, ^{16}O + ^{93}Nb, and ^{13}C + ^{93}Nb were obtained using the first and second methods as described in the text. The lines are drawn just to guide the eyes.

$\alpha_{charge} = \frac{(Z_T - Z_P)}{(Z_T + Z_P)}$ is the charge asymmetry, and the symbols have their usual meanings. Our recent studies found that ICF probability increases with the entrance channel mass asymmetry of the projectile-target combinations [33, 37]. However, in addition to mass asymmetry, the charge asymmetry of the system is also expected to have an impact on the ICF dynamics. Therefore, the individual mass asymmetry effect cannot be used as a parameter for observing the overall asymmetry effects of the entrance channel on ICF dynamics, as stated by Morgenstern et al. [39] and other researchers [23, 24, 31]. Hence, the incorporation of charge asymmetry along with mass asymmetry is necessary to fully explain the dynamics of ICF. Apart from that, in order to reach a definitive conclusion on this point, the present study on low-energy ICF dynamics has considered the charge asymmetry with the entrance channel mass-asymmetry of the system. Thus, the deduced ICF fraction F_{ICF}(%) for the present system ^{16}O + ^{93}Nb has been compared with those obtained for ^{16}O-induced reactions with ^{51}V [34], ^{115}In [61], ^{159}Tb [62], ^{165}Ho [36], and ^{175}Lu [63] targets at the constant relative velocity (V_{rel} = 0.053c) as a function of the α_{total} parameter in Fig. 9(a). From this graph, it can be noted that the ICF fraction increases with the total asymmetry parameter.

D. ICF dependence on system parameter ζ

In our recent studies [34, 37], we have discussed the role of the Coulomb factor (Z_PZ_T) in ICF dynamics and found that the Coulomb factor may play a vital role in the breakup of the projectile. The semiclassical or classical techniques are more suitable and effective when dealing with situations that involve considerable angular momentum and smaller wavelengths. The semiclassical treatment is applicable when the Sommerfeld parameter is significantly greater than one. Therefore, the semiclassical treatment can be used to comprehend the dynamics of the reaction. The Sommerfeld parameter is explained as

$$\eta = \frac{Z_P Z_T e^2}{4\pi\epsilon_o \hbar \upsilon}$$

The symbols have their usual meanings. The relative velocity υ can be written as $\upsilon = \sqrt{2E_{c.m.}}/\sqrt{\mu}$. Thus, the Sommerfeld parameter can be rewritten as

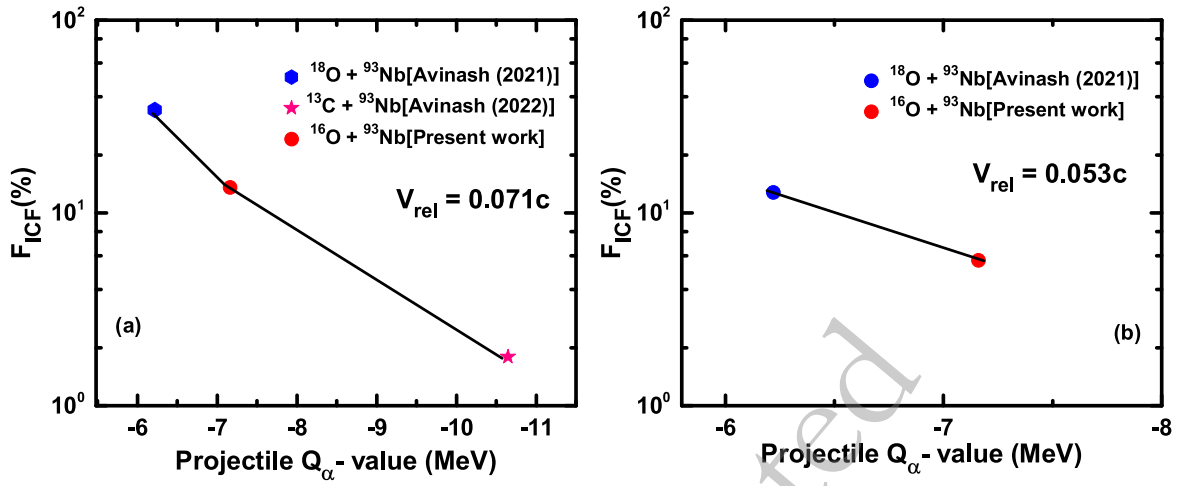

Fig. 8. (color online) (a) The deduced incomplete fusion fraction F_{ICF}(%) is shown as a function of the projectile Q_α value at a constant relative velocity V_{rel} = 0.071c. (b) The deduced F_{ICF}(%) is shown as a function of the projectile Q_α value at a constant relative velocity V_{rel} = 0.053c. The ^{13}C + ^{93}Nb system has not been included here because reliable ICF fraction data for this system at V_{rel} = 0.053c are not available in the literature. The lines drawn are just to guide the eye.

$$\eta = 0.1575 \times Z_P Z_T \sqrt{\frac{\mu}{E_{c.m.}}}$$

Here, $\mu = \frac{A_P A_T}{(A_P + A_T)}$ is the reduced mass of the projectile-target combinations. The Sommerfeld parameter can now be defined as follows:

$$\eta = \frac{0.1575 \star \zeta}{\sqrt{E_{c.m.}}}$$

Here, the symbol $\zeta = Z_P Z_T / \sqrt{\mu}$ is called the "system parameter." From the above expression, it is evident that the system parameter ζ is directly proportional to the charge product $Z_P Z_T$ and inversely proportional to the square root of the reduced mass μ. Since the Sommerfeld parameter η is proportional to $\zeta / \sqrt{E_{c.m.}}$, the system parameter effectively governs the relative strength of Coulomb repulsion compared to the kinetic energy of the interacting nuclei. A larger value of ζ implies stronger Coulomb interaction and comparatively lower relative acceleration of the system due to increased inertia. Under such conditions, the projectile experiences enhanced Coulomb stress in the interaction region, which may increase the probability of its breakup prior to complete fusion. Therefore, ζ encapsulates both the Coulomb repulsion and the dynamical inertia of the entrance channel, making it a physically meaningful scaling parameter for understanding the breakup–fusion competition and the observed variation of F_{ICF}. Further, to observe the ICF's reliance on this system parameter, which appears to be a more comprehensive parameter (as it includes the Coulomb factor as well as the masses of the interacting partners) compared to the above-discussed parameters, the values of F_{ICF}(%) for the present system ^{16}O + ^{93}Nb, along with those obtained for ^{16}O induced reactions with ^{51}V [34], ^{115}In [61], ^{159}Tb [62], ^{165}Ho [36], and ^{175}Lu [63] targets, have been shown against the system parameter ζ at a constant V_{rel} in Fig. 9(b). This figure indicates that the ICF fraction increases with the system parameter. Moreover, the system parameter ζ, which takes into account the Coulomb factor ($Z_P Z_T$) and the mass dependence of the interacting partners, is a suitable parameter for comprehending the dynamics of the ICF reaction at low energies.

E. ICF dependence on fissility parameter χ

The incorporation of ICF events, as well as other reaction mechanisms such as fission and quasifission, may elevate the difficulty of synthesizing superheavy materials [64, 65]. The main objective of the present study is to investigate exactly how the features of the interacting partners affect the ICF reactions and, of course, to identify the trends that can be summarized into a systematic framework. Fissility is a measure of the stability of charged liquid droplets. It is a valuable theory first proposed by Lord Rayleigh [66] and then applied by Niels Bohr [67] to atomic nuclei, leading to the development of the theory of nuclear fission based on the liquid drop model (LDM). Therefore, to comprehend the impact of the fissility parameter on the ICF reactions, we have plotted the F_{ICF}(%) values for the presently studied system, along with results obtained for ^{16}O induced reactions with ^{51}V [34], ^{115}In [61], ^{159}Tb [62], ^{165}Ho [36], and ^{175}Lu [63] targets, at a constant relative velocity V_{rel} = 0.053c as shown in Fig. 10. It can be seen from this figure that the F_{ICF}(%) increases with the fissility parameter (χ) for projectile-target combinations, and this trend seems to mirror the total asymmetry parameter dependence of the ICF

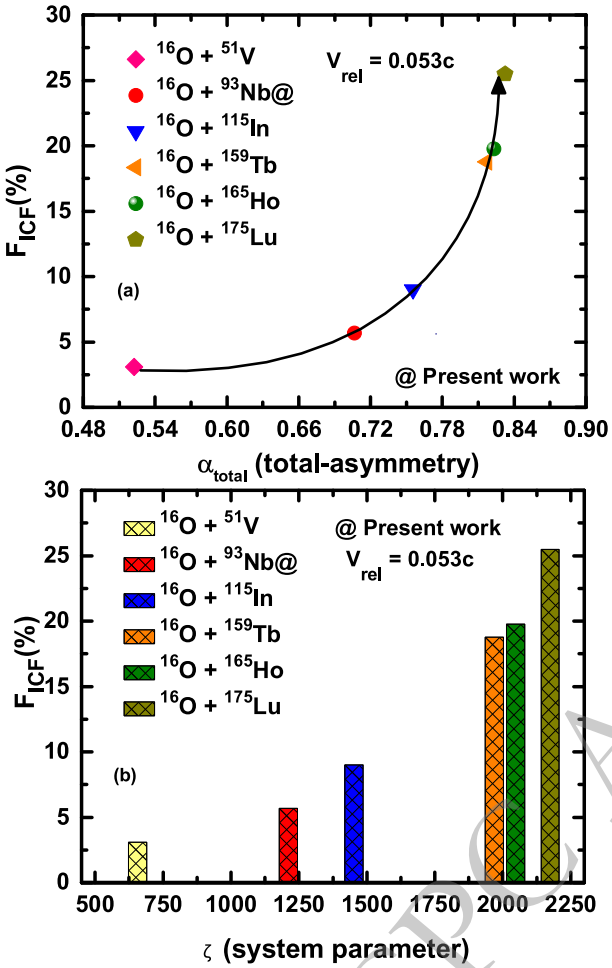

Fig. 9. (color online) The deduced incomplete fusion fraction F_{ICF}(%) for the ^{16}O-induced reaction with ^{51}V, ^{93}Nb, ^{115}In, ^{159}Tb, ^{165}Ho, and ^{175}Lu targets is presented as a function of entrance channel parameters: (a) the total asymmetry parameter α_{total}, and (b) the system parameter (ζ) at a constant relative velocity (V_{rel} = 0.053c). Refer to the text for further details.

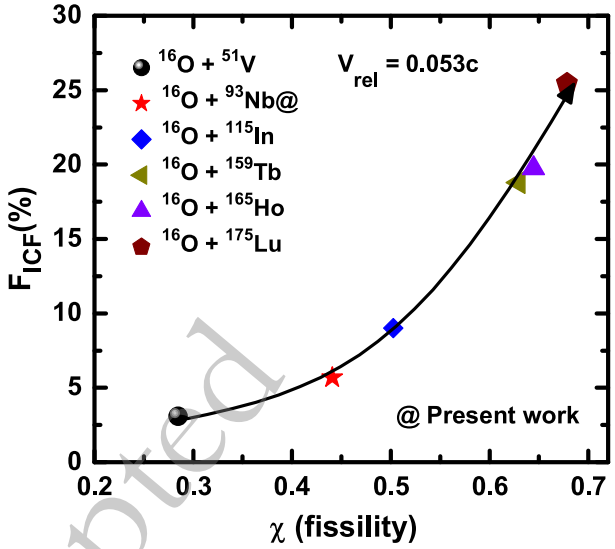

Fig. 10. (color online) The deduced incomplete fusion fraction F_{ICF}(%) for the ^{16}O-induced reaction with ^{51}V, ^{93}Nb, ^{115}In, ^{159}Tb, ^{165}Ho, and ^{175}Lu targets is presented as a function of the fissility parameter (χ) at a constant relative velocity (V_{rel} = 0.053c). The line is included merely to guide the eyes. Refer to the text for further details.

Table 4. Nuclear potential parameters, i.e., potential depth (V_0), radius parameter (r_0), and diffuseness (a_0) for different reactions calculated using NRV [68] and ICF fraction F_{ICF}(%) at a constant relative velocity (V_{rel} = 0.053c).

System	V_0(MeV)	r_0(fm)	a_0(fm)	F_{ICF}(%)	Ref.
Projectile: ^{16}O					
^{93}Nb	−58.25	1.174	0.644	5.69	#
^{159}Tb	−62.79	1.177	0.653	18.79	[62]
^{175}Lu	−63.58	1.178	0.655	25.47	[63]
Projectile: ^{18}O					
^{93}Nb	−58.72	1.175	0.648	12.78	[37]
^{159}Tb	−62.58	1.178	0.657	27.39	[69]
^{175}Lu	−63.30	1.178	0.659	30.78	[63]

reactions.

F. ICF dependence on nuclear potential parameters

The knowledge of nuclear potential is fundamental to any nuclear reaction. Different mechanisms of nuclear reactions are introduced by interpreting the outgoing channels in terms of various entrance-channel parameters, e.g., energy, mass, structural properties, and nuclear potential. The nuclear potential parameters, i.e., potential depth (V_0), radius (r_0), and diffuseness (a_0), have been shown to influence the reaction dynamics, including incomplete fusion, albeit having some peculiar characteristics that differ from system to system. To justify the effect of nuclear potential parameters on incomplete fusion, nuclear potential parameters for various reactions have been estimated using Winther nuclear potential [68], and are presented in Table 4. The systems are the same as given in the previous subsection. As the mass of target nuclei increases, the values of nuclear potential parameters and ICF probability increase individually for ^{16}O and ^{18}O projectiles. The reason may be that the nuclear potential tends to attract more incoming particles, but it is unable to capture them all due to the increase in diffuseness, which reduces the sharpness of nuclear potential at the surface. The input angular momentum of the projectile drastically increases owing to the combined increase in radius and radius parameter. As both sharpness and input angular momentum increase simultaneously, the whole projectile cannot be captured by the attractive potential of the target nuclei. Therefore, complete fusion gives way to incomplete fusion to provide sustainable input angular

momentum.

G. Role of target deformation parameter (β_2)

This subsection describes the role of target deformation on the dynamics of the ICF for low projectile energies. The deformation parameter (β_2) is related to the quadrupole moment of a nucleus (Q_0), which in turn explains the nucleus shape. Inamura et al. [70] found that peripheral interactions are mostly responsible for ICF processes. Therefore, the change in ICF fraction may be understood on the basis of the target deformation parameter. In view of these aspects, the deduced F_{ICF} for the present system $^{16}O+^{93}Nb$ has been compared with the earlier studied systems $^{16}O+^{115}In$ [61], $^{16}O+^{159}Tb$ [62], and $^{16}O+^{175}Lu$ [63] and plotted against the target deformation parameter (in Fig. 11) at the same relative velocity 0.053c. The values of the deformation parameter (β_2) are taken from Ref. [71]. Detailed information about the formulation of the deformation parameter (β_2) is given in Ref. [72]. It can be observed from Fig. 11 that F_{ICF}(%) increases with the increase in the deformation parameter (β_2), as also mentioned in the study of Singh et al. [73]. The present work indicates that the nucleus deformation parameter (β_2) may also play an essential role in ICF reaction dynamics along with projectile structure.

H. Universal fusion function: Effect of projectile break-up on complete fusion cross sections

In order to study the breakup effects of strongly bound projectiles (^{18}O, ^{16}O, and ^{13}C, which have higher break-up thresholds) on the fusion cross-section at energies above the Coulomb barrier, we further employed the UFF methodology in this analysis. This method, proposed by Canto et al. [4], aims to reduce fusion data by eliminating geometrical parameters such as radii and barrier heights, as well as the static effects of the potential between two interacting nuclei. To calculate the reduced cross-section and collision energy, one must use the reduction procedure in the form

$$\sigma_{CF} \rightarrow F(x) = \frac{2E_{c.m.}}{R_b^2\hbar\omega}\sigma_{CF}, \qquad E \rightarrow x = \frac{E_{c.m.} - V_b}{\hbar\omega}$$

Here, $\hbar\omega$, R_b, and V_b are the barrier curvature, radius, and barrier height, respectively, while $E_{c.m.}$ is the energy in the center of mass frame, and σ_{CF} is the fusion cross-section. These dimensionless fusion cross-sections were termed fusion functions F(x). The reduction of the fusion cross-section to the fusion function F(x) is calculated using the Wong formula [74].

$$\sigma_F^W(E_{c.m.}) = \frac{R_b^2\hbar\omega}{2E_{c.m.}} \ln\left[1 + \exp\left(\frac{2\pi(E_{c.m.} - V_b)}{\hbar\omega}\right)\right].$$

On simplifying the Wong formula, $F(x)$ reduces to

$$F_0(x) = \ln[1 + exp(2\pi x)],$$

Note that the above fusion function is a general function of the dimensionless variable x, $F_0(x)$, which does not depend on the system. For this reason, it was called the Universal Fusion Function in Ref. [4]. It is important to mention that the only limitation of Wong's formula is that it fails to represent the sub-barrier fusion cross section of lighter nuclei. However, this study deals with projectile energies much larger than the Coulomb barrier, where Wong's formula can be applied. In the present work, the experimental fusion functions (EFFs) are deduced for three systems, viz., ^{16}O + ^{93}Nb (present work), ^{18}O + ^{93}Nb [37], and ^{13}C + ^{93}Nb [33], and plotted against the dimensionless variable x as shown in Fig. 12. The EFFs have been obtained using the experimentally measured fusion cross sections (σ_{sum}^{CF}) for the above-mentioned systems. The solid lines in Fig. 12 represent the UFF, which was calculated using the prescription in Ref. [4]. It is evident from this figure that the CF function is observed to be suppressed below the UFF line for all the given systems. The suppression of complete fusion observed from the comparison with the UFF prediction can be directly related to the presence of incomplete fusion processes identified in the present work. In reactions involving cluster-structured projectiles, breakup in the vicinity of the barrier diverts a fraction of the incoming flux away from the complete fusion channel. This lost flux does not disappear but instead contributes to partial fusion processes, which are experimentally observed as incomplete fusion residues. The extracted FICF values

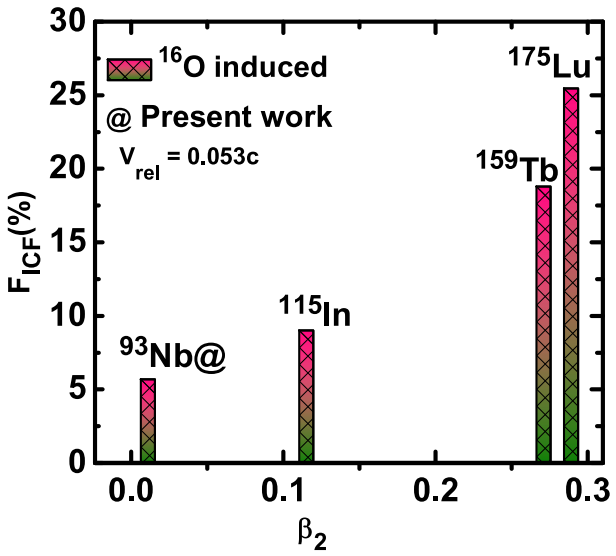

Fig. 11. (color online) The variation of incomplete fusion fraction F_{ICF}(%) with target deformation (β_2) at a relative velocity, $V_{rel} \approx 0.053c$. Refer to the text for details.

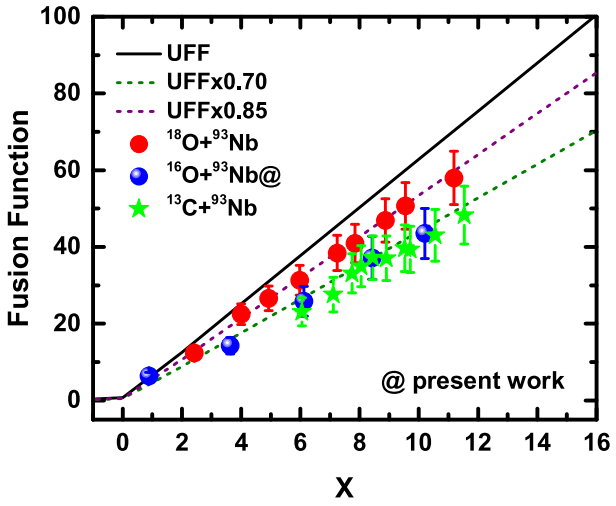

Fig. 12. (color online) Fusion function $F(x)$ as a function of x for ^{18}O, ^{16}O (present work), and ^{13}C induced reactions on a ^{93}Nb target. The solid black curve is the benchmark UFF curve (see text for details). The two dotted curves are the UFF curve multiplied by 0.85 and 0.70.

therefore represent a redistribution of reaction flux that would otherwise contribute to complete fusion. It is noteworthy that the magnitude and energy dependence of the observed CF suppression are consistent with the trend of the ICF component. Similar flux-diversion mechanisms leading to CF suppression have been discussed in recent publications [4, 29]. Moreover, the data for all systems are within the range of the UFF curve multiplied by 0.70 to 0.85, implying CF suppression of 15% to 30%.

V. SUMMARY AND CONCLUSION

Fusion cross-section measurements have been carried out for the ^{16}O + ^{93}Nb system at energies ranging from 55.1 to 98.1 MeV using the activation technique along with off-line γ-ray spectroscopy. The experimentally measured EFs have been compared with the statistical model PACE4 code to shed light on their production mechanism. The results of previous work [41] on the same system, ^{16}O + ^{93}Nb, are compared to the findings of the present study. Cavinato et al.'s [55] formalism has been used to calculate the independent cross-sections of some ERs fed by their higher charge precursor isobars. The measured EFs of ERs populated through x*n* and/or *pxn*-emitting channels are found to be in good agreement with the predictions of the theoretical code, indicating their production via CF only over the studied energy regime. However, the measured production cross-sections of ERs populated via α-emitting channels significantly exceed their theoretical predictions, which may be associated with an incomplete fusion process. Furthermore, a comprehensive analysis of the present work along with literature data reveals that the incomplete fusion fraction greatly depends on entrance channel parameters. To understand the influence of projectile structure on ICF, the total fusion cross-sections of systems ^{18}O + ^{93}Nb, ^{16}O + ^{93}Nb, and ^{13}C + ^{93}Nb have been reduced using two different procedures. It has been noticed that the reduced total fusion cross-sections for ^{18}O are larger than those of the ^{16}O and ^{13}C projectiles with the ^{93}Nb target. These present results show that the ICF contribution of ^{16}O is larger than that of ^{13}C and less compared to the ^{18}O projectile, which may be explained on the basis of the Q_α value. Additionally, to gain insight into the entrance channel total-asymmetry effect on ICF dynamics, the F_{ICF}(%) values of the present study are compared with other existing systems in the literature. The present work shows that the ICF probability increases exponentially with entrance channel total-asymmetry. Furthermore, the ICF strength function has been measured in terms of the system parameter. The system parameter ζ, which encompasses the Coulomb factor (Z_PZ_T) and the mass dependence of the interacting partners, appears to be an adequate parameter for comprehending the ICF reaction dynamics at these low energies. It has also been noted that the probability of ICF is sensitive to the fissility parameter, nuclear potential parameters, and target deformation. To gain a better understanding of the effect of projectile break-up on fusion cross-section at projectile energies above the Coulomb barrier, the fusion function F(x) derived from the total CF cross-section data for the ^{18,16}O and ^{13}C-induced reactions has been compared with the universal fusion function. A significant total CF suppression was observed, which is assigned to the prompt breakup of the projectiles. Moreover, the results obtained in the present study are significant and may be useful for improving the understanding and modeling of ICF reaction dynamics at low energies.

ACKNOWLEDGEMENTS

The authors are grateful to the Director of IUAC, New Delhi, for providing all the necessary resources for conducting the experiments. One of the authors, A.A., is thankful to the Council of Science and Technology, U.P. (CST-UP), Lucknow, INDIA, for financial support through research project ID-4890. A. K. Jashwal acknowledges the Ministry of Social Justice & Empowerment, Government of India, for providing a research fellowship, ref. no. 44-1/2018(SA-III), 5262. The authors express their thanks to Prof. V. P. Singh, Head of the Physics Department, Bareilly College Bareilly (India), for his motivation and support. The authors wish to thank the technical staff of IUAC for the operation of the Pelletron and their cooperation during the course of this experiment.

References

[1] N. Rowley, K. Hagino, Phys. Rev. C **91**, 044617 (2015)
[2] L.R. Gasques, D.J. Hinde, M. Dasgupta, A. Mukherjee, R.G. Thomas, Phys. Rev. C **79**, 034605 (2009)
[3] M. Dasgupta *et al*., Phys. Rev. Lett. **82**, 1395 (1999)
[4] L.F. Canto, P.R.S. Gomes, J. Lubian, L. Chamon, E. Crema, Nucl. Phys. A **821**, 51 (2009)
[5] P.R.S. Gomes, J. Lubian, I. Padron, R.M. Anjos, Phys. Rev. C **71**, 017601 (2005)
[6] P.P. Singh, B.P. Singh, M.K. Sharma, Unnati, D.P. Singh, R. Prasad, Phys. Rev. C **77**, 014607 (2008)
[7] M.K. Sharma, Unnati, B.K. Sharma, B.P. Singh, H.D. Bhardwaj, R. Kumar, K.S. Golda, R. Prasad, Phys. Rev. C **70**, 044606 (2004)
[8] P. Vergani, E. Gadioli, E. Vaciago, E. Fabrici, E. Gadioli Erba, M. Galmarini, G. Ciavola, C. Marchetta, Phys. Rev. C **48**, 1815 (1993)
[9] A. Ojha, S. Gupta, U. Gupta, P.P. Singh, A. Yadav, D.P. Singh, Mohd Shuaib, B.P. Singh, R. Prasad, Phys. Rev. C **104**, 034615 (2021)
[10] H. Timmers, D. Ackermann, S. Beghini, L. Corradi, J.H. He, G. Montagnoli, F. Scarlassara, A.M. Stefanini, N. Rowley, Nucl. Phys. A **633**, 421 (1998)
[11] M. Dasgupta *et al*., Phys. Rev. C **70**, 024606 (2004)
[12] K. Hagino, Phys. Rev. C **98**, 014607 (2018)
[13] D.J. Hinde, R.G. Thomas, R. du Rietz, A. Diaz-Torres, M. Dasgupta, M.L. Brown, M. Evers, L.R. Gasques, R. Rafiei, M.D. Rodriguez, Phys. Rev. Lett. **100**, 202701 (2008)
[14] A.B. Balantekin *et al*., Rev. Mod. Phys. **70**, 77 (1998)
[15] A.M. Stefanini *et al*., Phys. Rev. C **78**, 044607 (2008)
[16] K.E. Rehm *et al*., Phys. Rev. Lett. **81**, 3341 (1998)
[17] A.M. Vinodkumar *et al*., Phys. Rev. C **87**, 044603 (2013)
[18] C. Signorini, Nucl. Phys. A **616**, 262 (1997)
[19] A. Gomez Camacho, A. Diaz-Torres, H.Q. Zhang, Phys. Rev. C **99**, 054615 (2019)
[20] H.D. Marta, L.F. Canto, R. Donangelo, Phys. Rev. C **89**, 034625 (2014)
[21] Y.D. Fang *et al*., Phys. Rev. C **87**, 024604 (2013)
[22] A.K. Jashwal, A. Agarwal, H. Vardhan, I.A. Rizvi, R. Kumar, A.K. Chaubey, Eur. Phys. J. Plus **138**, 1069 (2023)
[23] P.K. Giri *et al*., Phys. Rev. C **100**, 024621 (2019)
[24] Mohd Shuaib *et al*., J. Phys. G: Nucl. Part. Phys. **44**, 105108 (2017)
[25] C.S. Palshetkar, S. Santra, A. Chatterjee, K. Ramachandran, S. Thakur, S.K. Pandit, K. Mahata, A. Shrivastava, V.V. Parkar, V. Nanal, Phys. Rev. C **82**, 044608 (2010)
[26] C. Signorini *et al*., Phys. Rev. C **67**, 044607 (2003)
[27] A. Di Pietro *et al*., Phys. Rev. C **85**, 054607 (2012)
[28] A. Pakou *et al*., Phys. Rev. C **102**, 031601(R) (2020)
[29] A. Diaz-Torres, D.J. Hinde, J.A. Tostevin, M. Dasgupta, L.R. Gasques, Phys. Rev. Lett. **98**, 152701 (2007)
[30] A. Diaz-Torres, I.J. Thompson, Phys. Rev. C **65**, 024606 (2002)
[31] S.A. Tali *et al*., Phys. Rev. C **100**, 024622 (2019)
[32] E.Z. Buthelezi *et al*., Nucl. Phys. A **734**, 553 (2004)
[33] A. Agarwal *et al*., Phys. Rev. C **105**, 034609 (2022)
[34] M. Kumar, A. Agarwal, S. Prajapati, K. Kumar, S. Dutt, I.A. Rizvi, R. Kumar, A.K. Chaubey, Phys. Rev. C **100**, 034616 (2019)
[35] M. Gull, K. Kumar, S. Ali, T. Ahmad, S. Dutt, I.A. Rizvi, A. Agarwal, R. Kumar, Phys. Rev. C **98**, 034603 (2018)
[36] K. Kumar, T. Ahmad, S. Ali, I.A. Rizvi, A. Agarwal, R. Kumar, K.S. Golda, A.K. Chaubey, Phys. Rev. C **87**, 044608 (2013)
[37] A. Agarwal *et al*., Phys. Rev. C **103**, 034602 (2021)
[38] D.J. Parker, J.J. Hogan, J. Asher, Phys. Rev. C **39**, 2256 (1989)
[39] H. Morgenstern, W. Bohne, W. Galster, K. Grabisch, A. Kyanowski, Phys. Rev. Lett. **52**, 1104 (1984)
[40] O.B. Tarasov, D. Bazin, Nucl. Instrum. Methods Phys. Res. B 266 (2008) 4657; A. Gavron, Phys. Rev. C 21 (1980) 230; http://lise.nscl.msu.edu/pace4.
[41] A. Sharma, B.B. Kumar, S. Mukherjee, S. Chakrabarty, B.S. Tomar, A. Goswami, S.B. Manohar, J. Phys. G: Nucl. Part. Phys. **25**, 2289 (1999)
[42] The stopping and range of ions in matter (SRIM) code, http://www.srim.org/SRIM/SRIMLEGL.htm.
[43] CANDLE, Data acquisition and analysis software, Inter University Accelerator Centre (IUAC), New Delhi, India.
[44] E. Browne, R.B. Firestone, Table of Radioactive Isotopes, Wiley, New York, 1986.
[45] W. Hauser, H. Feshbach, Phys. Rev. **87**, 366 (1952)
[46] R. Bass, Phys. Rev. Lett. **39**, 265 (1977)
[47] D. Wilmore, P.E. Hodgson, Nucl. Phys. A **55**, 673 (1964)
[48] F.D. Becchetti, G.W. Greenlees, Phys. Rev. **182**, 1190 (1969)
[49] J.P. Lestone, Phys. Rev. C **53**, 2014 (1996)
[50] A. Gilbert, A.G.W. Cameron, Can. J. Phys. **43**, 1446 (1965)
[51] Y.D. Fang *et al*., Phys. Rev. C **91**, 014608 (2015)
[52] D. Singh *et al*., Pramana J. Phys. **82**, 683 (2014)
[53] B.B. Kumar, S. Mukherjee, S. Chakrabarty, B.S. Tomar, A. Goswami, S.B. Manohar, Phys. Rev. C **57**, 743 (1998)
[54] A. Chauhan, M. Maiti, S. Lahiri, Phys. Rev. C **99**, 064609 (2019)
[55] M. Cavinato, E. Fabrici, E. Gadioli, E. Gadioli Erba, P. Vergani, M. Crippa, G. Colombo, I. Redaelli, M. Ripamonti, Phys. Rev. C **52**, 2577 (1995)
[56] A. Yadav, V.R. Sharma, P.P. Singh, D.P. Singh, M.K. Sharma, U. Gupta, R. Kumar, B.P. Singh, R. Prasad, R.K. Bhowmik, Phys. Rev. C **85**, 034614 (2012)
[57] O. Akyz, A. Winther, in: R.A. Broglia, R.A. Ricci, C.H. Dasso (Eds.), Proc. Int. School of Physics Enrico Fermi, Course LXXVII, North-Holland, Amsterdam, 1981, p. 492.
[58] K. Ikeda, H. Horiuchi, and S. Saito, Prog. Theor. Phys. Suppl. **68**, 1 (1980)
[59] K. Kumar, T. Ahmad, S. Ali, I.A. Rizvi, A. Agarwal, R. Kumar, A.K. Chaubey, Phys. Rev. C **89**, 054614 (2014)
[60] A. Yadav *et al*., Phys. Rev. C **107**, 044605 (2023)
[61] K. Kumar, T. Ahmad, S. Ali, I.A. Rizvi, A. Agarwal, R. Kumar, A.K. Chaubey, Phys. Rev. C **88**, 064613 (2013)
[62] M.K. Sharma *et al*., Nucl. Phys. A **776**, 83 (2006)
[63] H. Kumar, Ph.D. Thesis, A.M. University, Aligarh, India, 2017.
[64] A.C. Berriman *et al*., Nature **413**, 144 (2001)
[65] R.N. Sagaidak, M.L. Chelnokov, V.I. Chepigin, V.A. Gorshkov, O.N. Malyshev, A.G. Popeko, A.I. Svirikhin, A.V. Yeremin, Phys. Rev. C **105**, 024604 (2022)
[66] L. Rayleigh, Philos. Mag. **14**, 184 (1882)
[67] N. Bohr, J. Wheeler, Phys. Rev. **56**, 426 (1939)
[68] http://nrv.jinr.ru/nrv/webnrv/fusion/.
[69] A. Yadav *et al*., EPJ Web Conf. **117**, 08022 (2016)
[70] T. Inamura, M. Ishihara, T. Fukuda, T. Shimoda, H. Hiruta, Phys. Lett. B 68 (1977) 51; T. Inamura, A.C. Kahler, D.R. Zolnowski, U. Garg, T.T. Sugihara, M. Wakai, Phys. Rev. C 32 (1985) 1539.
[71] P. Moller, J.R. Nix, W.D. Myers, W.J. Swiatecki, At. Data Nucl. Data Tables **59**, 185 (1995)
[72] S. Raman, C.W. Nestor Jr., P. Tikkanen, At. Data Nucl. Data Tables **78**, 1 (2001)
[73] D. Singh *et al*., Phys. Rev. C **97**, 064610 (2018)
[74] C.Y. Wong, Phys. Rev. Lett. **31**, 766 (1973)